

Supplementary Material for Montel et al.

1 SIZE DISTRIBUTION

The droplets were made using a SPG membrane with pores of 10 μm diameter, yielding a reproducible size distribution. The threshold of $r < 9 \mu\text{m}$ for particle detection in our image analysis corresponds to the smallest droplets in the size distribution.

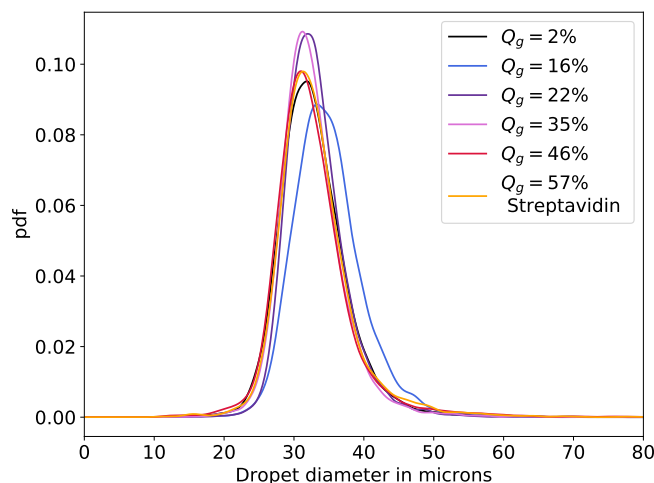


Figure S1. *Droplet size distribution* — Distribution of droplet diameters for each experimental condition.

2 IMAGE ANALYSIS

2.1 Segmentation

For each experiment, a sample of 3-5 images at different packing fractions is used to classify pixels between background and foreground using a Random Forest Algorithm with Ilastik (see an example of a raw image in Figure S2A). The selected features are the following : Color/Intensity 1 - 3.5 -10 σ , Edge 0.7-1-1.6-3.5 σ , Texture 1-1.6-3.6 σ . Examples of foreground and background pixels are selected manually until the classifier can correctly predict the contour of the droplets, independently of their color, as shown on Figure S2B. The resulting binary segmented image is then skeletonized using Fiji to obtain the droplet boundaries.

2.2 Voronoi cells

Fiji's Analyze Particles module is used to detect objects larger than 1500 pixels ($76 \mu\text{m}^2$) and with a circularity above 0.6. A surface voronoi tessellation is then performed on the binary mask of these objects, as demonstrated in Figure S2C.

2.3 Contact network

The droplet boundary image obtained after segmentation is labeled and measured using the scikit-image Python package. All objects with an area below 5000 pixels (i.e. with a radius $r < 9 \mu\text{m}$) or a circularity lower than 0.5 are discarded. Here the threshold is more permissive than for the droplet contour analysis because we do not exclude droplets touching the border from the contact analysis, lest we underestimate the number of contacts per droplet near the boundary. We then use the `future.graph.rag_boundary` function

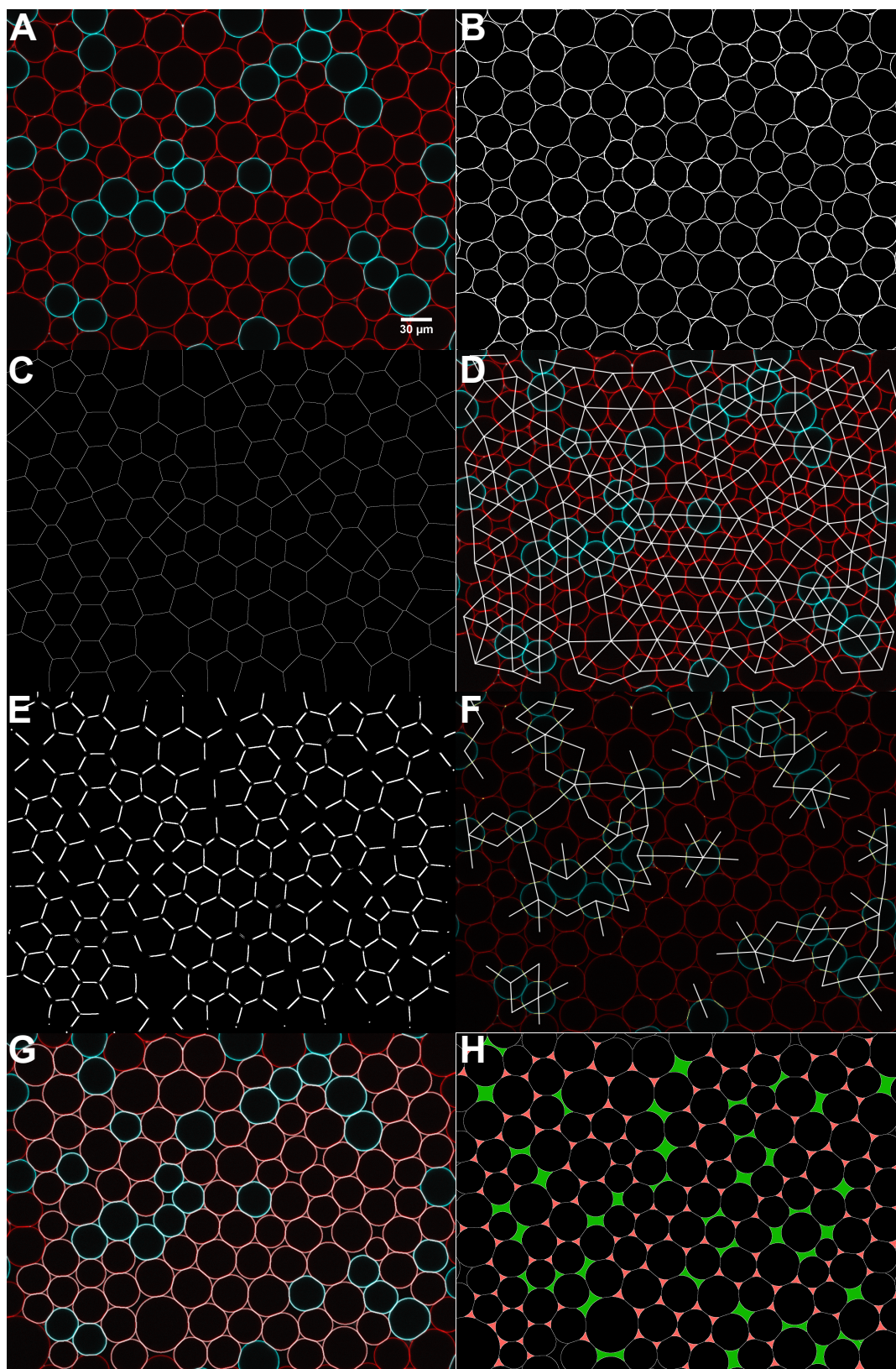


Figure S2. *Image analysis steps* — (A) : Confocal image of functionalized DNA complementary droplets. (B) : Droplets segmented by Ilastik. (C) : Surface Voronoi tessellation by Fiji. (D) : Network of contacts by Region Adjacency Graphs. (E) : Patch searching areas. (F) : Detected patches (in yellow) and adhesive patches network. Patches below $1\mu\text{m}^2$ are discarded from the analysis as they correspond to aggregates on the droplets. (G) : Droplet contours smoothed with a Savitzky-Golay filter for perimeter and area measurements. (H) : Voids classification, 3-sided voids in light red, 4-sided voids in green.

of the scikit-image package to generate a graph of the connected labeled regions. An example of graph is shown on Figure S2D. This graph is then used to compute the number of contacts z for each droplet. The droplets whose Voronoi cells touch the border of the images are excluded from the analysis of z , since the total count of their contacts cannot be obtained from the image.

2.4 Patch detection

The intersection between the voronoi cells and droplet boundaries identifies the contact area between two droplets. Thus, we multiply the binary segmentation obtained from Ilastik (S2B) and the binary Voronoi tessellation (S2C) dilated twice, to obtain a binary image of the zone where we should look for patches (S2E). Images of complementary DNA droplets have two fluorescent channels, corresponding to Alexa-488 and Alexa-555. For each color, we define an intensity threshold $I_{thres} = 1.5(\langle I \rangle + 2\sigma(I))$, where $\langle I \rangle$ is the average intensity on the image, and $\sigma(I)$ is its standard deviation. We measured that the intensity $(\langle I \rangle + 2\sigma(I))$ corresponds well the intensity at the surface of droplets on the image. The histogram of intensity can be seen on Figure S4. The 1.5 multiplier was chosen by trial and error to best reflect the patches as observed by eye.

The detected patches are visible in yellow on Figure S2F. Small yellow areas are detected and correspond to local protein aggregates. To exclude them from patch analysis, we discard patches with an area below $1\mu\text{m}^2$. For each detected patch, we reference the labels of the two associated droplets. The contact network extracted from 2.3 is coupled with the patch detection to yield a graph of adhesive contacts, i.e. contacts displaying a patch at the droplet-droplet interface, as illustrated in white on S2F. The number of adhesive contacts z_a are counted for each droplet and used to compute the local adhesiveness Q_l .

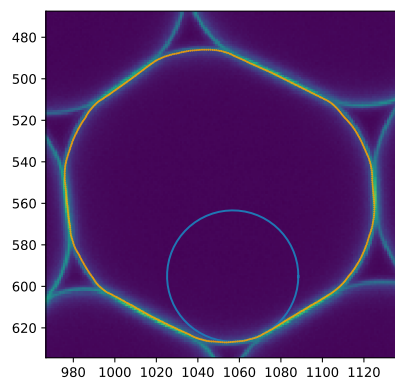


Figure S3. *Smoothing of a droplet contour* — Smoothed contour of a droplet (orange) and local osculating circle computed from the contour (blue).

2.5 Area and perimeter measurements

Area and perimeter measurements can be impacted by the pixelization of the images. To avoid overestimating the perimeter, and thus the deformation, we approximate the local shape of the droplets by arcs of circles. From the droplet boundary image, we label each object larger than 1500 pixels and with a circularity above 0.67 as a droplet and extract its contour. We exclude from the shape analysis all the droplets touching the borders of the image. The contour is smoothed with a Savitzky-Golay filter (with a window of 13 points and linear fit). An example of the smoothed contours can be seen on Figures S2G and S3. For each point i of the contour, we find the fitting osculating circle between the $(i-6)$, i and the $(i+6)$ points and approximate the shape of the droplets with these arcs of circles. The perimeter p is computed as

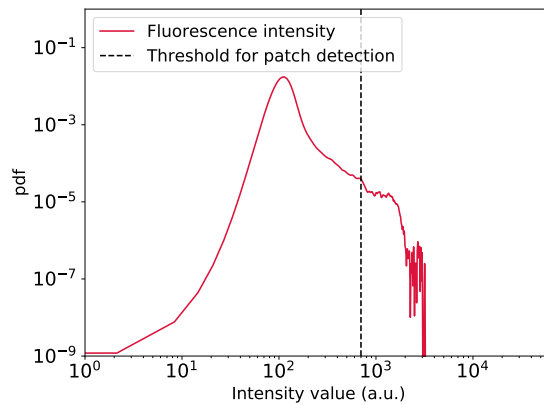


Figure S4. *Determination of the patch detection threshold* — Histogram of intensity in the red channel of the confocal image presented on Figure S2 A. The threshold for patch detection is chosen as $1.5(\langle I \rangle + 2\sigma(I))$, where $\langle I \rangle$ is the average intensity, and $\sigma(I)$ is the standard deviation.

the sum of the length of the arcs. The area of the polygon formed by every sixth point of the contour is computed, then the area of the supplementary arcs of circles is added to the area to obtain the area of the droplet. The shape parameter $\mathcal{A} = \frac{p^2}{4\pi a}$ is then calculated for each droplet. The local packing fraction ρ is the ratio between the area a and the area of the corresponding Voronoi cell.

3 ADHESIVENESS

The local adhesiveness of a droplet $Q_l = \frac{z_a}{z}$ is the ratio between z_a the number of contacts with an adhesive patch, and the total number of contacts of this droplet. As a ratio between integers that are typically <6 , it can take a limited number of values between 0 and 1. The cumulative distribution of Q_l within each experimental condition is presented on figure S5.

The global adhesiveness Q_g is the averaged Q_l over one experimental condition.

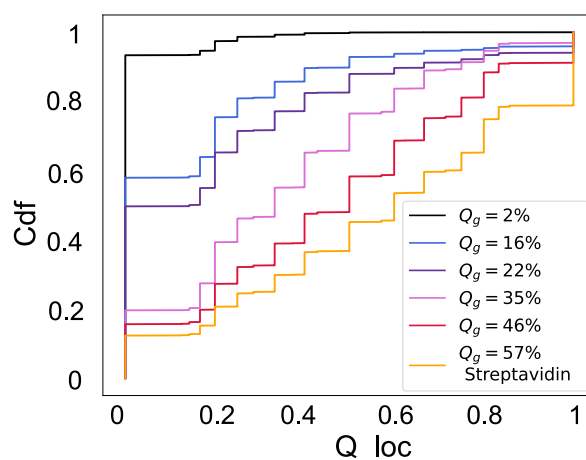


Figure S5. *Adhesiveness distribution* — Cumulative probability distribution of the local adhesiveness Q_l for the varying global adhesiveness Q_g .

For each experimental condition, we binned the droplets by local adhesiveness Q_l and plotted the shape parameter $\mathcal{A} - 1$ as a function of ρ on Figure 6 of the main text. For each binned curve, we computed the least-squares measures

$$\chi^2(\rho) = \frac{(\mathcal{A}(\rho) - \mathcal{A}_{repulsive}(\rho))^2}{\mathcal{A}_{repulsive}(\rho)}$$

and plotted it on Figure S6A-C. The total sum of χ^2 over all ρ values is plotted as a function of the local adhesiveness Q_l on Figure S6D-F. There is no significant difference between droplets with different local adhesiveness Q_l within an emulsion of a given global adhesiveness Q_g . Thus, the relationship between shape and packing fraction appears to be a global property of an adhesive emulsions, depending only on its global adhesiveness Q_g .

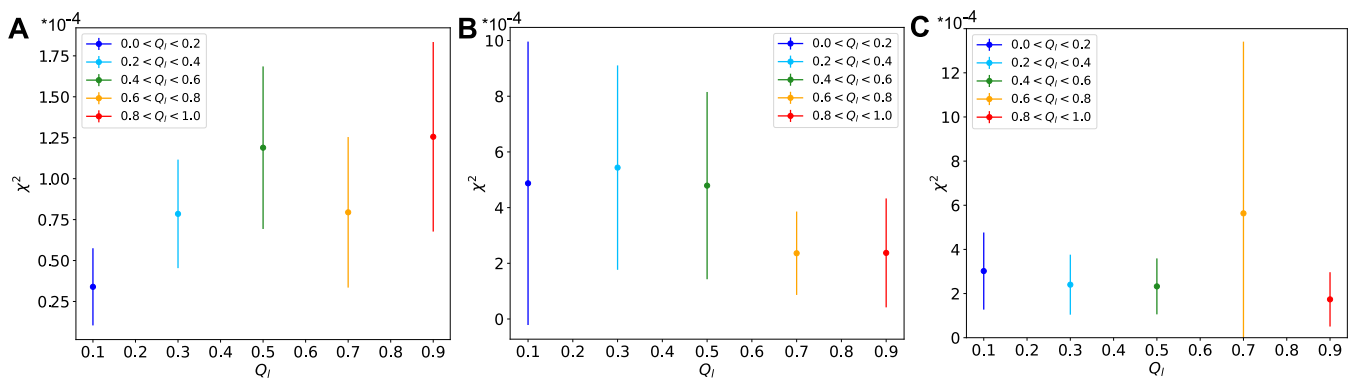


Figure S6. Droplet local adhesiveness — (A-C) χ^2 computed between each group of Q_l and the repulsive control for DNA packings yielding a global adhesiveness $Q_g = 35\%$ (A), $Q_g = 46\%$ (B), and in streptavidin packings yielding $Q_g = 57\%$ (C)

4 STRUCTURAL PROPERTIES

A number of early computational studies of the jamming transition focused on the investigation of the mechanical and rheological properties of packings of soft (but non deformable) spheres, in which the potential energy cost is related to the overlap between pairs of particles [1, 2, 3, 4]. In particular, it was shown that the excess coordination

$$z - z_c \sim (\phi - \phi_c)^\alpha, \quad (\text{S1})$$

obeys a power-law scaling with the distance to the jamming onset $\phi - \phi_c$, where the scaling exponent is $\alpha = 0.5$ [1, 2]. In this scaling relation, ϕ represents the packing fraction in the sense of a *reduced number density* which is not the true packing fraction which we measure in our experiments. It is defined as $\phi = \sum_{i=1}^N \pi \sigma_i^2 / 4A$, where σ_i is the diameter of disk i and A is the area of the confining box.

A number of experimental studies focused on the structural and mechanical properties of repulsive emulsions in 2D and 3D [5, 6, 7, 8]. Experimentally, it was found that the excess coordination obeys the following power-law scaling

$$z - z_c \sim (\rho - \rho_c)^\beta, \quad (\text{S2})$$

where $0.4 \leq \beta \leq 1$ and ρ is the *true* packing fraction. While for both definitions $\rho_c = \phi_c$, a notorious problem with soft sphere models is that particles remain spherical and do not conserve area when the packings are compressed above jamming onset; as a consequence, $\phi > \rho$ above jamming onset. This is in

contrast with actual emulsions in which droplets are incompressible and thus maintain their area (volume) during compression over the whole range of compression $\rho_c \leq \rho \leq 1$. In particular, droplets can deform and form additional contacts which may explain some of this discrepancy in scaling exponents. In an effort to address the limitations of the soft sphere models, a recent study showed using a model of deformable particles [9, 10] that the excess coordination was better captured by the following relation

$$z - z_c \approx z_0(\rho - \rho_c)^\alpha + z_1(\rho - \rho_c)^\beta, \quad (\text{S3})$$

where $z_c = 4$, $\rho_c \approx 0.84$, $\alpha = 0.5$ and $\beta = 1.0$.

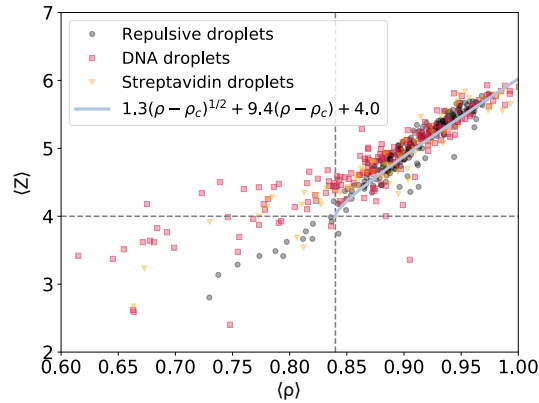


Figure S7. *Global coordination in jammed emulsions* — shown as a function of the global packing fraction $\langle \rho \rangle$ for emulsions made of repulsive droplets (black circles), droplets DNA functionalization (red squares) and droplets with streptavidin-biotin functionalization (yellow triangles). The data for repulsive emulsions is well-fitted by Equation S3. Dashed lines correspond to the jamming transition for 2D repulsive packings at $\rho_c = 0.84$ and $z_c = 4$.

The data for repulsive droplets is in qualitative agreement with the proposed model. However, the accuracy on the experimental data, especially very close to ρ_c , is not sufficient to confirm the scaling.

5 FORCE BALANCE MODELLING

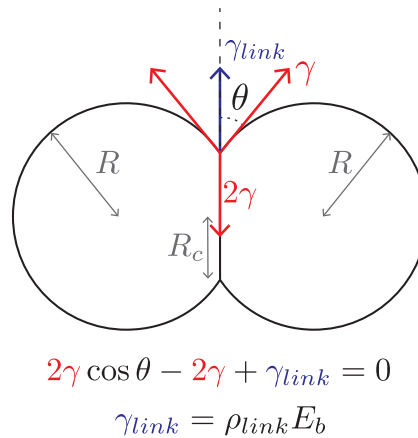


Figure S8. Sketch of the force balance model used to extract the density of binders in the patch.

We model doublets of droplets as passive materials exhibiting a surface tension at the oil-water interface γ and a surface tension at the contact interface γ_i , as illustrated on Fig. S8. Assuming that the composition in phospholipids is homogeneous over the entire droplets, we defined $\gamma_i = \gamma - \frac{\gamma_{link}}{2}$, where γ_{link} is the surface tension contribution coming from the bound linkers. Defining the binding energy per bond as E_b , one can also write $\gamma_{link} = \rho_{link}E_b$, where ρ_{link} is the average binder density in the patch [11]. We focus on packings of DNA droplets at the highest adhesiveness $Q_g = 46\%$ so that they are comparable to streptavidin droplet packings at $Q_g = 57\%$ and analyze the average patch in these packings below jamming so that the droplets are uncompressed.

REFERENCES

- [1] O'Hern CS, Silbert LE, Liu AJ, Nagel SR. Jamming at zero temperature and zero applied stress: The epitome of disorder. *Phys. Rev. E* **68** (2003) 011306. doi:10.1103/PhysRevE.68.011306.
- [2] O'Hern CS, Langer SA, Liu AJ, Nagel SR. Random packings of frictionless particles. *Phys. Rev. Lett.* **88** (2002) 075507. doi:10.1103/PhysRevLett.88.075507.
- [3] Durian DJ. Foam mechanics at the bubble scale. *Phys. Rev. Lett.* **75** (1995) 4780–4783. doi:10.1103/PhysRevLett.75.4780.
- [4] Lacasse MD, Grest GS, Levine D, Mason TG, Weitz DA. Model for the elasticity of compressed emulsions. *Phys. Rev. Lett.* **76** (1996) 3448–3451. doi:10.1103/PhysRevLett.76.3448.
- [5] Desmond KW, Young PJ, Chen D, Weeks ER. Experimental study of forces between quasi-two-dimensional emulsion droplets near jamming. *Soft Matter* **9** (2013) 3424–3436. doi:10.1039/C3SM27287G.
- [6] Jorjadze I, Pontani LL, Brujic J. Microscopic approach to the nonlinear elasticity of compressed emulsions. *Phys. Rev. Lett.* **110** (2013) 048302. doi:10.1103/PhysRevLett.110.048302.
- [7] Jorjadze I, Pontani LL, Newhall KA, Brujic J. Attractive emulsion droplets probe the phase diagram of jammed granular matter. *Proceedings of the National Academy of Sciences of the United States of America* **108** (2011) 4286–4291.
- [8] Katgert G, van Hecke M. Jamming and geometry of two-dimensional foams. *EPL (Europhysics Letters)* **92** (2010) 34002. doi:10.1209/0295-5075/92/34002.
- [9] Boromand A, Signoriello A, Ye F, O'Hern CS, Shattuck MD. Jamming of deformable polygons. *Phys. Rev. Lett.* **121** (2018) 248003. doi:10.1103/PhysRevLett.121.248003.
- [10] Boromand A, Signoriello A, Lowensohn J, Orellana CS, Weeks ER, Ye F, et al. The role of deformability in determining the structural and mechanical properties of bubbles and emulsions. *Soft Matter* **15** (2019) 5854–5865. doi:10.1039/c9sm00775j.
- [11] Maître JL, Berthoumieux H, Krens SFG, Salbreux G, Jülicher F, Paluch E, et al. Adhesion functions in cell sorting by mechanically coupling the cortices of adhering cells. *Science* (2012). doi:10.1126/science.1225399.